ORR activity and stability of carbon supported Pt<inf>3</inf>Y thin films in PEMFCs

Electrochimica Acta 472 (2023) 143436

Contents lists available at ScienceDirect

Electrochimica Acta

journal homepage: www.journals.elsevier.com/electrochimica-acta

ORR activity and stability of carbon supported Pt_3Y thin films in PEMFCs

Eva Marra [a,*], Gerard Montserrat-Sisó [b], Björn Eriksson [a], Björn Lönn [b], Rakel Wreland Lindström [a], Göran Lindbergh [a], Björn Wickman [b], Carina Lagergren [a]

[a] Department of Chemical Engineering, KTH Royal Institute of Technology, SE-100 44 Stockholm, Sweden
[b] Department of Physics, Chalmers University of Technology, SE-412 96 Gothenburg, Sweden

ARTICLE INFO

Keywords:
Proton exchange membrane fuel cell
Platinum rare earth metal alloy
Platinum yttrium thin film
Oxygen reduction reaction
Accelerated stress test

ABSTRACT

In order to investigate stability of oxygen reduction reaction (ORR) on a Pt_3Y thin film under relevant fuel cell conditions, we performed an accelerated stress test (AST) consisting of 3600 potential cycles between 0.4 and 1.4 V at 1 V s^{-1} in a single proton exchange membrane fuel cell (PEMFC). The ORR activities were evaluated via polarization curves before and after the AST. Electrochemical active surface area (ECSA) was obtained by CO-stripping voltammetry whereas the morphological changes were monitored by means of scanning electron microscopy (SEM) and transmission electron microscopy (TEM). Variations in surface composition and electronic structures were evaluated by energy-dispersive X-ray spectroscopy (EDX) and X-ray photoelectron spectroscopy (XPS). After AST, the polarization curves show loss of ORR activity in all voltages for both Pt and Pt_3Y. Except at very high voltages ($E > 0.85$ V_{RHE}), the ORR activity of Pt_3Y after AST is very close to that of Pt before AST. This correlates well with the results from the deconvolution of Pt-4f XPS spectra where the binding energy of metallic Pt in Pt_3Y is comparable to pure Pt (71.22 eV). SEM and TEM images demonstrate that the morphologies of the aged Pt_3Y and as-sputtered Pt are similar, whereas EDX results confirm a steady bulk composition of Pt_3Y thin films throughout the entire electrochemical test. By correlating all these results, we conclude that the loss of ORR activity for Pt_3Y is due to an increase in the thickness of the Pt overlayer which induces a relaxation of the Pt overlayer decreasing the compressive strain effect. For pure Pt, the loss of ORR activity is associated with a growth of the Pt domains associated with Ostwald ripening process.

1. Introduction

Proton exchange membrane fuel cells (PEMFCs) are crucial devices in the decarbonization of transport systems because of their lightweight, low-temperature operation and high energy density [1,2]. Nevertheless, the widespread commercialization of PEMFCs in fuel cell vehicles is currently hindered by their high cost and limited lifetime, which is greatly attributed to the large amounts of Pt required to catalyze the sluggish kinetics of the oxygen reduction reaction (ORR) at the cathode [3]. In that respect a lot of PEMFC research has focused on decreasing the Pt loading through either microstructuring [4–6] or alloying with other metals [7–9].

Alloying Pt with rare earth metals (Pt-REMs) depicts a promising and competitive alternative to increase the activity of pure Pt while reducing the cost of the cathode layer. In addition of being highly active for the ORR, Pt-REMs have a low alloy formation energy, which makes them thermodynamically stable in acidic conditions compared to Pt alloyed with other late transition metals [10]. Based on theoretical calculations [11,12] and experimental results [13,14], there is a solid consensus that the increased ORR activity observed in Pt-REM electrodes arises from a compressive strain effect on the Pt overlayer induced by the Pt-REM bulk, where the incorporation of REM atoms deforms the closely packed Pt lattice and thus lowers the interatomic distance between Pt atoms at the overlayer. The resulting changes in the electronic structure of Pt modify the binding energy towards oxygen-containing species (OCS) [15], which in turn facilitates the electroreduction of the hydroxyl radical (HO*), an unavoidable intermediate that inhibits the ORR [12,13,16]. Sputtered Pt_3Y films have been proven to be effective catalysts for the ORR in acidic media. In rotating disk electrode (RDE) measurements, the reported ORR specific activities are 7 times higher compared to that of pure Pt [17–20], whereas in fuel cell conditions, our group reported a specific ORR activity enhancement of around 2.5 times at 0.9 V_{RHE} in a membrane electrode assembly (MEA) setup [21,22]. Moreover, our measurements revealed only minor changes in the Pt_3Y surface

* Corresponding author.
E-mail address: emarra@kth.se (E. Marra).

https://doi.org/10.1016/j.electacta.2023.143436
Received 12 July 2023; Received in revised form 11 October 2023; Accepted 30 October 2023
Available online 31 October 2023

composition after exposure to fuel cell MEA conditions, which suggests reasonable stability under potential cycling in acidic media. Thus, given the current interest in incorporating this Pt-alloy as an actual PEMFC cathode catalyst, its morphological and electrochemical stability during long-time performance need to be evaluated for obtaining accurate PEMFC lifetime predictions.

The ORR catalyst stability in PEMFCs is complex and time-consuming to evaluate. In transport applications, the dynamic operating conditions and the long-term stability target of thousands of hours are impractical when performing lab-scale tests. Accelerated stress tests (ASTs) have been developed to simulate different degradation mechanisms affecting PEMFC electrocatalysts during operation [23]. A commonly used AST is based on triangular wave potential perturbations [23–25], where the stability of Pt-Y alloys has mainly been investigated between 0.6 and 1.1 V in RDE tests [16,17,26,27], far from real fuel cells degradation conditions. Alternatively, cycling the potential between 1 and 1.5 V with a high sweep rate simulate startup and shutdown conditions, which have an important influence on catalyst stability [28]. In addition to catalyst degradation under these conditions, the cathode potential may be sufficiently high to induce intense carbon corrosion, which becomes more severe when the electrode potential is actively changing [29,30]. In this scenario, extended electrochemical tests of Pt_3Y in relevant PEMFC conditions, especially cycling up to 1.5 V, remains elusive.

By virtue of all considerations above, we performed an AST consisting of 3600 potential cycles between 0.4 and 1.4 V at a sweep rate of 1 V s^{-1} in a single PEMFC for investigating the long-term stability of Pt_3Y thin films under relevant fuel cell conditions. Prior to electrochemical measurements, Pt_3Y electrodes were acid-treated in order to induce the formation of the Pt skin overlayer [21]. The impact of the AST on ORR activities was evaluated by performing polarization curves before and after AST. These results were then normalized with the electrochemical surface area (ECSA) obtained from CO-stripping voltammetry. The morphological changes of both Pt- and Pt_3Y thin films upon AST tests were monitored by means of scanning electron microscopy (SEM) and transmission electron microscopy (TEM), whereas changes in their surface compositions and in their electronic structures were evaluated by energy-dispersive X-ray spectroscopy (EDX) and X-ray photoelectron spectroscopy (XPS). Based on the obtained results, this AST methodology has been useful for demonstrating that Pt_3Y after AST tends to perform as Pt before AST in relevant fuel cell conditions. As such, the proposed protocol is expected to be of great use for future AST studies when characterizing the stability of Pt-alloys in PEMFC.

2. Experimental

2.1. Sputtered thin films of Pt and Pt_3Y

Pt_3Y and Pt thin films were fabricated using a Nordiko 2000 sputter coater using pure Pt and Pt_3Y alloy targets. The gas diffusion layer (GDL) used in all experiments was Carbel CL (230 μm thick). All GDLs were Ar^+ plasma cleaned in situ prior to deposition. Before sample deposition, the Pt_3Y target was pre-sputtered for at least 2 min to remove surface oxides on the target. The pure Pt target was pre-sputtered for 1 min. The base pressure of the Nordiko 2000 was lower than 1.0×10^{-6} mbar with a working gas pressure of 6.6 mbar under 50 sccm (standard cubic centimeters per minute) of Ar gas flow. The resulting Pt- and Pt_3Y films deposited onto the GDL had a nominal thickness of 60 nm, corresponding to a Pt loading of 128.8 and 99.6 μg cm^{-2}, respectively.

2.2. Double-MEA assembly

The sputtered Pt_3Y film on GDL was punched to obtain a circular gas diffusion electrode (GDE) of 0.95 cm^2 geometrical area. In order to remove impurities (i.e., yttrium oxides) from the thin film surface, the GDE was pretreated as follows: immersion in 0.1 M $HClO_4$ (perchloric acid) for 15 min and subsequent washing with Mili-Q water. This procedure was repeated three times and the GDE was subsequently dried for 30 min at room temperature. The circular catalyst film was assembled together with a Nafion 212 membrane and a commercial MEA, both square shaped (4 × 4 cm). Finally, a Sigracet 25BC (235 μm thick) GDL of 3 cm^2 was used at the anode. This configuration has been used previously and will be referred to as a double-MEA setup [21,22]. The Pt_3Y film acted as a working electrode (WE), while one catalyst layer of the commercial MEA (furthest from the WE) acted as a combined counter and reference electrode (CE/RE). The function of the Pt interlayer of the commercial MEA (closest to the WE) was to minimize H_2 crossover effect during electrochemical measurements and thus increase the accuracy in ORR activities at the low current-density region. The double-MEA setup and commercial PTFE gaskets were mounted inside a laboratory PEEK (polyether-etherketone) fuel cell, in between two cylindrical graphite current collectors having spirally-shaped gas flow channels. The assembled fuel cell was clamped by applying a clamping pressure of 5 bar. As further explained in the next section, the WE was fed with either O_2 or N_2 while the CE/RE worked with either H_2 or 5% H_2 balanced with Ar. Depending on the characterization step, the temperature of the cell was adjusted to 80 °C or 30 °C. All gases were humidified before entering the fuel cell. To avoid water condensation in the pipes between the humidifiers and the cell, their temperature was set to either 84 °C or 34 °C.

2.3. Electrochemical characterization

All electrochemical measurements were performed by connecting the cell to a PAR 273A potentiostat. The cathode was the working electrode (WE) while the anode performed as both counter and reference electrode (RE/CE). All potentials are referred to the Reversible Hydrogen Electrode (RHE).

The fuel cell was activated at 80 °C and 100% RH, supplying the WE and CE/RE with O_2 (14.8 ml min^{-1}) and H_2 (29.4 ml min^{-1}), respectively. The activation step consisted of 2000 potential cycles between 0.9 and 0.6 V at a sweep rate of 20 mV s^{-1}. Once this step was completed, the O_2 flow was lowered (7.4 ml min^{-1}) and the ORR activities were obtained by recording a sequence of potentiodynamic polarization curves between 0.9 and 0.3 V: first 50 sweeps at 20 mV s^{-1} and then 2 sweeps at 1 mV s^{-1}. Afterwards, potentiodynamic sweeps were performed with the same sweep rate but between 0.95 and 0.3 V, with O_2 (14.8 ml min^{-1}) at the WE and 5% H_2 balanced in Ar (300 ml min^{-1}) at the CE/RE. Considering Nernst equation, 5% H_2 balanced in Ar gives a voltage shift on the CE/WE of approximately 50 mV vs RHE. Hence, all results regarding performance at 80 °C have been corrected with this potential shift. The CO-voltammograms performed at 30 °C were corrected with a shift of 40 mV.

To obtain the ECSA, CO-stripping voltammetry was performed at 30 °C and 100% RH. Before starting, the entire system was flushed with N_2. The CO-stripping protocol involved the following four steps:

(I) Blank profile: cyclic voltammetry (5 cycles) between 0.05 and 1.2 V_{RHE}, at 200 mV s^{-1}. The WE operated with pure N_2 (100 ml min^{-1} and 100% RH) while on the CE/RE the gas was 5% H_2 balanced in Ar (100 ml min^{-1} and 100% RH). The conditions at the CE/RE were kept throughout the experiment.
(II) Potentiostatic CO adsorption: 2 min at 0.15 V by switching gas and feeding the WE channel with dry CO (2% in Ar).
(III) Purging the WE to remove remaining CO: shifting the inlet gas on the WE back to N_2 (100 ml min^{-1} and 100% RH) for 5 min.
(IV) CO-stripping voltammetry, performed at identical conditions as in (I).

2.3.1. Accelerated stress test (AST)

The stability of the WE was evaluated via an accelerated stress test

(AST) at 80 °C and 100% RH. The AST consisted of 3600 potential cycles between 0.4 and 1.4 V at 1 V s^{-1} sweep rate. The WE and CE/RE were provided with N_2 (100 ml min^{-1}) and 5% H_2 balanced in Ar (100 ml min^{-1}), respectively. The AST impact on ORR activities was then evaluated by repeating the sequence of polarization curves and CO-stripping voltammetry described earlier.

2.4. Physical characterization

Considering the electrochemical characterization described in the previous section, the nomenclature of the Pt_3Y samples characterized in this section follows a chronological order where: "as-sputtered" refers to a fresh thin-film Pt_3Y sample; "pre-treated" is a Pt_3Y sample which has been treated with $HClO_4$; "activated" refers to a pretreated Pt_3Y sample that after being assembled, has been subjected to electrochemical activation and finally; "aged" is the denomination for a Pt_3Y sample that, after activation, has passed through the AST test.

Scanning electron microscopy (SEM) coupled with energy-dispersive X-ray spectroscopy (EDX) was used to image and characterize the catalysts as-sputtered, acid treated, activated, and aged. SEM was performed using a Zeiss Supra 55VP field-emission microscope at 2 kV acceleration voltage and a working distance around 4 mm. EDX was performed in the same microscope with an IXRF spectroscopy unit. The working distance of the sample was increased to 23 mm and the acceleration voltage to 20 kV during EDX.

A PHI 5000 VersaProbe III Microprobe X-ray Photoelectron Spectroscopy (XPS) instrument (Physical Electronics) was used to study the surface composition of the sputtered Pt- and Pt_3Y thin films upon AST. The instrument is equipped with a monochromatic Al K-α X-Ray excitation source (1486.6 eV) operated at 50 W as well as a dual charge compensation: an electron neutralizer (negative charge compensation) and an ion gun (positive charge compensation). Surface composition was evaluated by a survey scan in the binding energy range between 0 and 1400 eV with an energy step width of 0.4 eV. The chemical states of Pt-4f, Y-3d, C-1 s and O-1 s core level spectra were studied in the narrow scan, which were recorded with an energy step of 0.1 eV and a pass energy of 69 eV. The measuring area was about 200 μm in diameter. The chamber pressure was always lower than 5.0×10^{-9} mbar during measurements. For all samples, the binding energy scale was corrected by shifting the spectra with respect to the Fermi level, which places adventitious C-1 s peak of the C=C bond to 284.4 eV (see Supplementary Information). Angle-resolved XPS was used in the same XPS instrument at three different angles (30°, 45° and 60°) and thus three different probing depths in order to track surface Pt and Y changes in terms of both composition and chemical state across the thin film. XPS measurements including angle-resolved XPS were performed for as-sputtered, acid-treated, activated and after AST for Pt_3Y samples, whereas for pure Pt XPS was performed on as-sputtered and after AST samples.

Transmission electron microscopy (TEM) imaging was performed to analyze the morphology of Pt_3Y thin film catalysts: as-sputtered, acid treated and after AST. The samples were prepared by scraping the outermost GDL layer containing the catalyst film, onto a water droplet, and the subsequent collection of fragments by gently brushing the water surface with a lacey carbon TEM grid. A FEI Tecnai T20 instrument, equipped with a LaB_6 filament and operating at 200 kV acceleration voltage, was used for the image acquisition.

3. Results and discussion

3.1. Electrochemical results

3.1.1. AST

Fig. 1 shows the AST consisting of 3600 cycles where the evolution of the cycles for Pt is shown in Fig. 1a and that for Pt_3Y in Fig. 1b. Regardless of the voltage, the magnitude of the current density for both

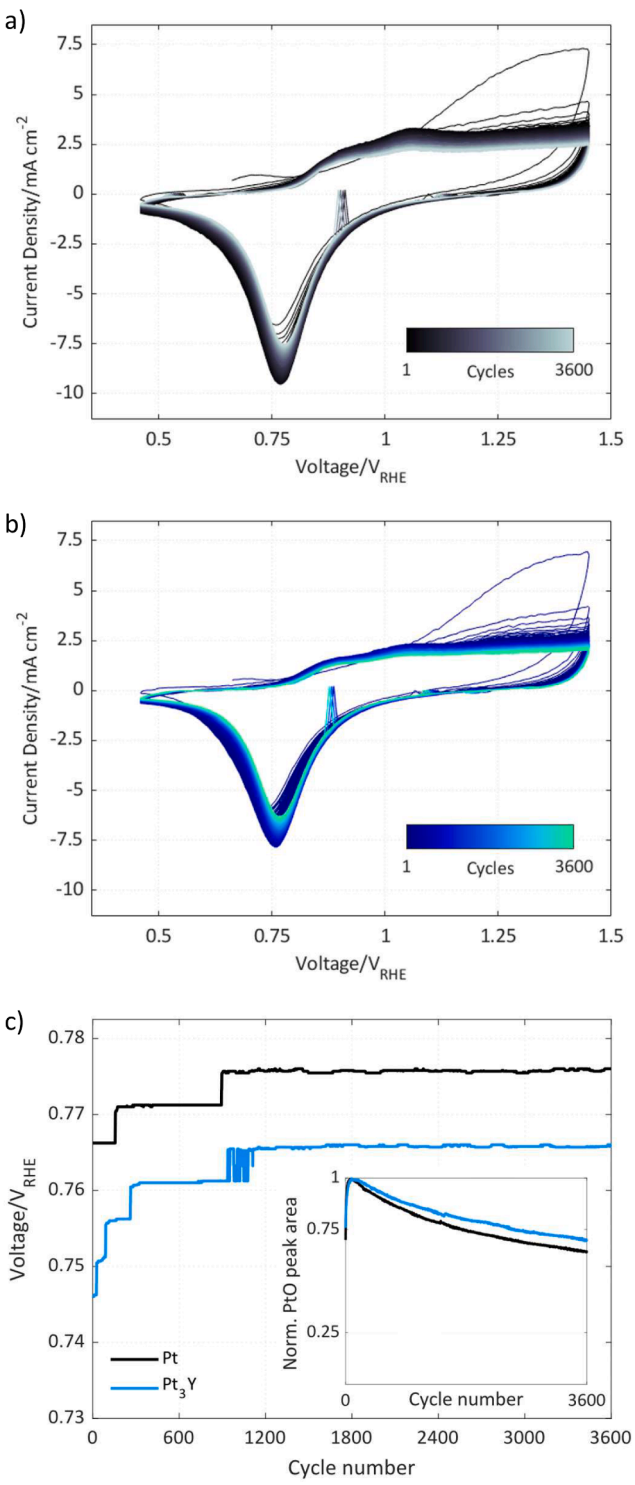

Fig. 1. Evolution of the AST for a) Pt and b) Pt_3Y. The AST consisted of 3600 potential cycles between 0.4 and 1.4 V_{RHE} at 1 V s^{-1} sweep rate. The WE and CE/RE worked with N_2 and 5% H_2 balanced in Ar respectively. c) Voltage location of the PtO reduction peak as a function of the number of cycles during the AST. The inset shows the evolution of the PtO peak area, normalized with respect to the maximum PtO peak area, reached after approximately 100 cycles.

Pt and Pt_3Y is reduced as the number of cycles progresses. This trend is more pronounced during the first 500 cycles and the PtO reduction peak decreases gradually in intensity. The PtO reduction peak is also shifted to higher voltages. Fig. 1c shows the voltage at which the PtO reduction peak is located along the 3600 cycles of the AST. For both catalyst

materials the shift of the PtO reduction peak toward higher voltages is more pronounced during the first cycles. As the number of cycles increases, the position of the PtO peaks of Pt and Pt_3Y stabilizes and the difference between them is reduced. The inset plot in Fig. 1c shows how the area of the PtO reduction peak changes along the AST. The PtO peak area was obtained by normalizing the actual area with respect to the maximum peak area, reached after approximately 100 cycles. For both catalysts the PtO peak area decreases around 30% from cycle 101 to 3600.

The shift of the PtO reduction peak to higher voltages is usually associated with an enhanced ORR rate due to a decrease of the Pt binding energy when adsorbing HO* [31]. However, Koper et al. have recently reported [32] that to assume this thermodynamic binding energy as a single descriptor for ORR rate may be erroneous. In order to be more accurate, they introduced a kinetic descriptor given by the reversible transition from O* to HO* (penultimate reaction step of ORR mechanism) which tracks the dependence of ORR rate on electrolyte. Hence, in addition to electrode surface, the ORR rate is also governed by the electrolyte effect and the PtO reduction peak results from a convolution of both descriptors. A deconvolution implies experimental difficulties due to this electrolyte-dependent kinetics that mainly applies for terrace (111) domains. However, it offers an alternative explanation to the counterintuitive relation between the shift of the PtO reduction peak and the observed ORR activities further explained in Section 3.1.3.

3.1.2. ECSA variation

The impact of AST on ECSA was evaluated by CO-stripping voltammetry and the results are shown in Fig. 2. The voltammograms for Pt and Pt_3Y are in Fig. 2a and 2b respectively. The ECSAs were calculated by integrating the area below the CO-electrooxidation peak, and by assuming 420 μC cm_{Pt}^{-2} as the charge required to oxidize the pre-adsorbed CO monolayer. The voltammogram for Pt before AST exhibits two tops: a main CO-electrooxidation peak centered at around 0.79 V_{RHE} and a shoulder at a lower voltage located at approximately 0.76 V_{RHE}. In the voltammetric profile for Pt after AST there is only a well-defined CO-electrooxidation peak, also centered at around 0.79 V_{RHE}. For Pt_3Y, both voltammograms display a single and well-defined CO-electrooxidation peak centered at around 0.77 V_{RHE}.

The peak position in voltammograms is a fingerprint of the particle size and electrode structure influenced by many factors such as crystallography of surface planes and surface defects [33,34]. All voltammograms have broad peaks indicating that the surfaces are not preferably oriented in a specific crystallographic plane. Urchaga et al. investigated the CO electrooxidation on polyoriented Pt nanosurfaces and, according to their conclusions [33], the shoulder we observe at around 0.76 V_{RHE} in the voltammetric profile for Pt before AST refers to a CO electrooxidation on well-ordered domains (terraces) while the main peak at approximately 0.79 V_{RHE} is ascribed to low-coordinated surface sites (steps). During the AST cycling conditions the order of terrace domains is broken and therefore, the single peak at around 0.79 V_{RHE} in the voltammogram for Pt after AST reflects a reconstructed surface [35] consisting of shorter terraces and steps where a change in size of the Pt domains is also involved [36,37]. Aside of the CO-stripping peak, the surface changes affect the entire voltammogram. In the case of Pt_3Y, the base voltammogram keeps stable and the peak observed at around 0.77 V_{RHE}, before and after AST, can be correlated to the peak for Pt at 0.79 V_{RHE} in Fig. 2a corresponding to low-coordinated surface sites. The changes in the electronic structure (d-band) when alloying Pt with Y lead to a weaker affinity for CO adsorption (weaker Pt–CO bond) [38] and therefore the CO-electrooxidation peaks on Pt_3Y electrode appears at lower voltages than for pure Pt.

For Pt, the ECSA decreases from 5.2 cm^2 (before AST) to 4.3 cm^2 (after AST) representing an ECSA loss of around 17% with respect to the initial area. For Pt_3Y the ECSA decreases from 3.6 cm^2 (before AST) to 3 cm^2 (after AST) corresponding to an ECSA loss of around 16% with respect to the initial area. As such, the obtained ECSA variation due to AST is similar in both catalyst materials. In $m^2 g_{Pt}^{-1}$ the ECSA of Pt decreases from 4.2 to 3.5 while for Pt_3Y this reduction is from 3.8 to 3.2 (see Supplementary information). These values are lower compared with the ECSAs obtained from conventional porous electrodes where Pt nanoparticles are dispersed forming a 3D Pt/C surface. In our case, the sputtered Pt thin films are model electrodes consisting of a simplified 2D architecture with lower ECSA but without the extra complications of non-uniform current distribution and mass transport limitations [39]. Except for Pt_3Y after AST, the CO-stripping protocol was in all cases repeated three consecutive times in order to ensure that the obtained ECSA values were stable. For Pt_3Y after AST (Fig. 2b), the protocol was repeated five times due to the instability of the CO peak. Ochal et al. [40] observed a similar behavior when using CO-stripping voltammetry for studying the nature of bimetallic RuPt core-shell architectures. According to their analysis the instability at the surface is attributed to a partial rearrangement of the surface as a consequence of AST (see Supplementary information).

3.1.3. Stability of Pt_3Y for ORR

Fig. 3 shows non-IR corrected steady-state polarization curves (before and after AST) for Pt and Pt_3Y. The measurements were repeated on different samples: a duplicate for Pt and a triplicate for Pt_3Y. In this

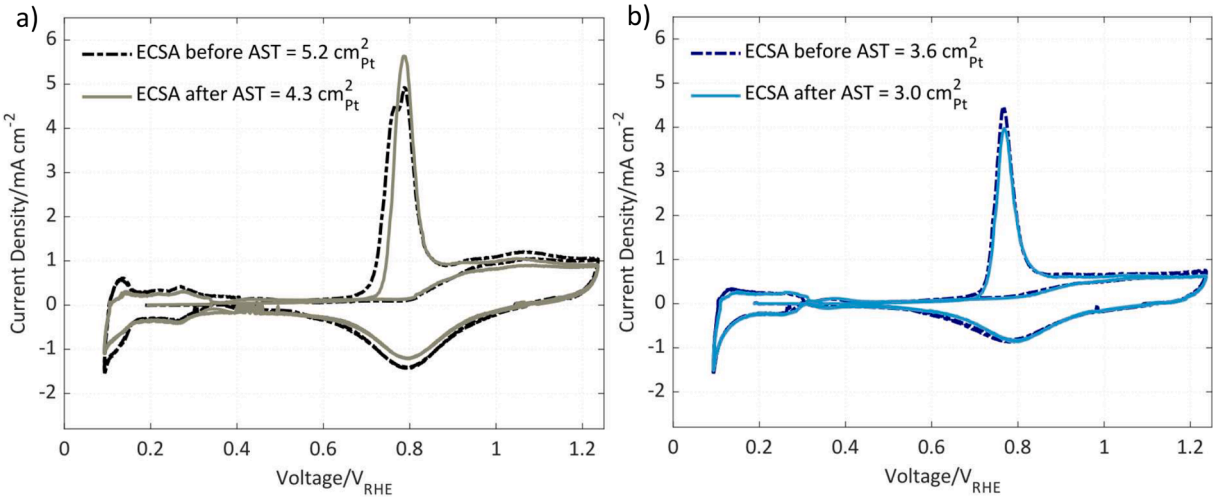

Fig. 2. CO voltammograms for a) Pt and b) Pt_3Y. The measurements were performed at 30 °C and 100% RH, with a scan rate of 200 mV s^{-1}. Except during the CO adsorption time, the system worked with N_2 (WE) and 5% H_2 balanced in Ar (CE/RE).

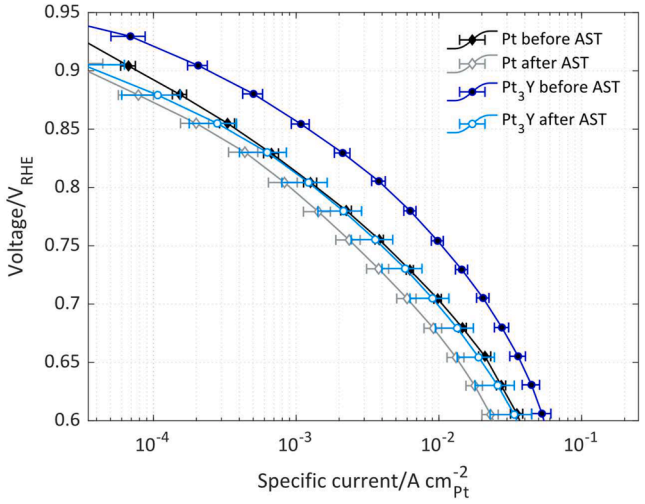

Fig. 3. Non-IR corrected steady-state polarization curves for Pt and Pt_3Y, before and after AST. The measurements were repeated on different samples: a duplicate for Pt and a triplicate for Pt_3Y. Each curve is the mean performance of the forward scans. The error bars represent the standard deviation. All measurements were performed at 80 °C and 100% RH and at 1 mV s^{-1} sweep rate. The setup worked with 100% O_2 (WE) and 5% H_2 balanced in Ar (CE/RE). .

context, every curve in Fig. 3 is the mean performance of the forward scans (the reverse scans are avoided in order to remove errors due to hysteresis phenomena). The mean performance curves including forward, and reverse scans are shown in the Supplementary information. The first recorded points were not stable and therefore they were excluded. The error bars represent the standard deviation, and the current densities were normalized with respect to the ECSA obtained from CO-stripping.

As a first observation, in agreement with previous studies commented in the introduction [21,22], once the electrodes are activated (before AST) the electrochemical performance of Pt_3Y film is higher than that of Pt. After the AST, the polarization curves for both electrode materials are shifted downwards indicating loss of ORR activity in all voltages considered. Except at very high voltages (E>0.85 V_{RHE}) in the low current-density region, the ORR activities of Pt_3Y after AST are very close to the ORR activities of Pt before AST. At E>0.85 V_{RHE} the ORR activities may have been affected by H_2 crossover as a consequence of minor changes in membrane thickness in combination with a degradation of the Pt interlayer forming the double-MEA setup [41,42]. Table 1 shows the ORR specific activities at 0.9 V_{RHE} ($i_{0.9}$ V_{RHE}) and 0.75 V_{RHE} ($i_{0.75}$ V_{RHE}) before and after AST. The ORR values were extracted via interpolation from the polarization curves in Fig. 3.

Before AST at 0.9 $V_{RHE,}$ the obtained specific ORR activity of Pt_3Y is roughly 3 times the ORR activity of Pt. This ratio decreases to around 1.2 after AST, which implies a reduction of the ORR specific activity of around 55% for Pt and 83% for Pt_3Y. At 0.75 $V_{RHE,}$ the obtained specific ORR activity of Pt_3Y before AST is around 2.5 times that of pure Pt, whereas after AST this ratio decreases to approximately 1.5, indicating a reduction of the ORR specific activities: around 40% for Pt and 60% for Pt_3Y. The ratios obtained before AST correlate very well with our previous studies [21,22]. The highest impact of the AST is for the ORR specific activities of Pt_3Y above 0.85 V_{RHE}. However, as mentioned before, these ORR activity values may have been influenced by H_2 crossover. Except for this region, a relative comparison of the ORR activities in Fig. 3 indicates that Pt_3Y after AST tends to perform as Pt before AST.

Table 1
Specific ORR activities at 0.9 V_{RHE} ($i_{0.9\ vRHE}$) and 0.75 V_{RHE} ($i_{0.75\ vRHE}$) extracted via interpolation from polarization curves in Fig. 3.

	ORR activities			
	Before AST		After AST	
	Pt	Pt_3Y	Pt	Pt_3Y
$i_{0.9}$ [μA cm_{Pt}^{-2}] ± standard deviation	76.5 ± 8.5	249.2 ± 40.7	34.0 ± 17.3	41.9 ± 32.7
$i_{0.75}$ [mA cm_{Pt}^{-2}] ± standard deviation	4.2 ± 0.3	10.5 ± 1.0	2.6 ± 0.5	4.0 + 1.3

For pure Pt, cycling conditions between 0.4 and 1.4 V in PEMFC systems are reported as highly detrimental [43]. Higashi et al. [42] investigated the degradation of Pt nanoparticles in a Pt/C cathode of a single PEMFC subjected to 300 start-up/shut-down cycles between 0.4 and 1.4 V_{RHE} via in-situ time-resolved quick X-ray absorption fine structure (QXAFS). Their results identified fractions of three kinds of Pt nanoparticles: active, less active, and inactive. It was found that, as the start-up/shut-down cycles progressed, the active Pt nanoparticles were transformed into less active and inactive. The less active fraction referred to Pt nanoparticles on thinner amorphous carbon layers with lower electronic conductivity and their ORR activity was estimated to be around 41 % of the active Pt nanoparticles. Interestingly, the resulting ECSA variation correlated with the sum of the fractions of the active and less active. The inactive sites are associated with dissolved Pt. In this context, Pavlišič et al. [44] have studied how the scan rate affects Pt dissolution and redeposition from a Pt/C during fuel cell cycling conditions. In this study, Pavlišič et al. showed that Pt redeposition is favored at high scan rates. This is due to faster kinetics; the Pt ions have less time to diffuse away and therefore there is a higher Pt-ion concentration near and on the catalyst thin film prone to be redeposited. In view of Higashi's and Pavlišič's results and considering our AST is more than ten times longer (3600 cycles), we conjecture that the decay in ORR activity we observe for pure Pt results from a restructuration of the Pt surface involving dissolution/redeposition process, where a high fraction of active Pt active sites is transformed into less active. The less active fraction contributes equally as active sites when measuring the ECSA and this is why the measured ECSA variation is not as significant as the decay in the ORR activity.

In the case of Pt_3Y, the ORR activities are strongly related to the structure of the Pt overlayer. Pedersen et al. [14] showed via X-ray diffraction that the overlayers of Pt_xY and Pt_xGd are strongly dependent on the electrochemical treatment they are exposed to. According to their RDE results, when cycling up to 1.3 V, the Pt overlayer in Pt_xY suffers a relaxation of the strain and loss of order causing a decrease of the ORR activities. The thickness of the Pt overlayer is an important variable since thicker Pt overlayers intensify the effect of strain relaxation [45]. Regarding Pt dissolution, the modified electronic structure of Pt_3Y attenuates the Pt dissolution. A previous study by Tang et al. [46] reported that the Pt dissolution from a nanoparticle occurs by direct electrooxidation of Pt to soluble Pt^{2+} cations. By performing DFT calculations, Jinnouchi et al. [47] studied the site-dependency of the direct Pt dissolution and concluded that Pt atoms with lower d-band centers are more resistant against dissolution. By correlating all these observations with the results from the physical characterization described in the next section, we deduce the decay in ORR activity for Pt_3Y after the AST is mainly due to a relaxation of the Pt overlayer.

3.2. Physical characterization

3.2.1. Bulk and surface composition

Pt- and Pt_3Y samples were physically characterized by energy-dispersive X-ray spectroscopy (EDX) which has a sensing depth in the micrometer range allowing the quantitative analysis of sputtered thin films bulk composition. Fig. 4 shows the EDX results, i.e., the Pt:Y bulk composition of Pt_3Y as-sputtered, acid treated, activated, and aged. The data reveal that the measured bulk composition is very close to that given by the nominal ratio of the sputtered target alloy (i.e., 3:1, dashed white line), although the ratio measured for the sputtered samples is slightly lower.

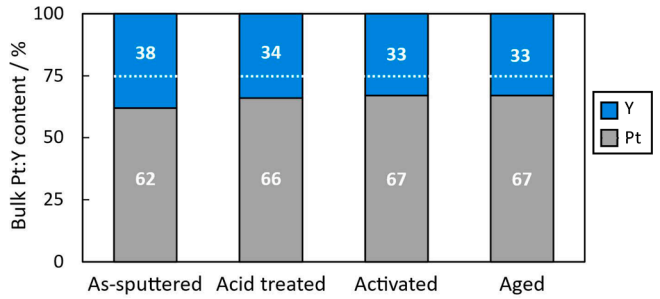

Fig. 4. Pt:Y bulk content, measured by EDX, for each Pt_3Y sample: as-sputtered, acid treated, activated, and aged. The dashed white line depicts the nominal Pt_3Y alloy composition of the sputtered targets (i.e., 3:1).

EDX confirms a steady bulk composition of Pt_3Y thin films throughout the entire electrochemical evaluation, which in turn indicates that the Pt-skeleton structure formed upon contact with acid does not affect the bulk composition. More importantly, the barely changing Pt:Y ratio in the bulk proves that the decay in ORR activity after aging cannot be ascribed to a complete leaching of Y atoms from the Pt-Y lattice.

The sputtered Pt_3Y thin films were also characterized by angle-resolved X-ray photoelectron spectroscopy (AR-XPS), whose angle-dependent surface-sensitive probing depth allows an accurate determination of surface elemental composition at different thin film depths. Considering the horizontal plane is at 0°, larger incident X-rays angle corresponds to a deeper region of the film being analyzed. Each Pt_3Y sample was measured at three different X-ray incident angles: 30°, 45° and 60° and the results are graphically shown in Fig. 5a (for numerical results see the Supplementary information). Moreover, the Y surface content was deconvoluted into metallic yttrium, Y^0 (light blue), and oxidized yttrium, Y^{3+} (dashed line pattern in blue), to further investigate the nature of surface species upon electrochemical testing.

In as-sputtered Pt_3Y thin film, the AR-XPS analysis revealed a surface-enrichment of Y^{3+}atoms compared to their nominal composition, which are believed to emerge to the surface due to their higher oxophilicity that makes Y more prone to undergo oxidation [20]. The surface enrichment with Y^{3+} in this sample is further evidenced by its higher Pt content at larger probing depths (i.e., 60°). As expected, the acid treatment results in a major depletion of surface Y atoms, which is greatly ascribed to the effective removal of yttrium oxides by $HClO_4$. Hence, given the ease in which Y oxidizes in contact with air and the amount of Y^0 observed in XPS, at this stage it is assumed that acid treatment effectively results in the formation of a Pt-rich surface overlayer [20,48,49]. Activation of Pt_3Y samples in acidic conditions gives rise to a further decrease in sub-surface Y, both metallic and oxide, which translates to a thickening of the Pt-skeleton structure. However, the slightly higher Pt content at lower angles may indicate the uncomplete removal of Y species on the surface. After AST, the aged sample exhibits an important decay in surface Y compared to the activated sample, which is mostly found as Y^0. The absence of surface Y^{3+}, together with the increase in amount of Pt at higher angles, confirm both the presence of subsurface Y^0 and the existence of a Pt overlayer after aging. However, despite the visible Y in the bulk, the XPS quantitative analysis alone is not capable to ensure that the bulk of the thin film is still alloyed in the aged sample.

XPS data may also be used for the calculation of the thickness of a film overlying onto another film at different angles. The variation in thickness of the Pt overlayer in Pt_3Y samples along electrochemical experiments was estimated from XPS data at 30° and the results are shown in Fig. 5b. Since in the as-sputtered sample the Pt:Y surface content is similar to the Pt:Y bulk content, this sample was excluded from the calculations (see Supplementary information). It should be mentioned that the thickness calculation assumes homogeneous and well-defined discrete films, which is most likely not the case in our samples and the trend rather than the absolute values should therefore be used for surface analysis. As explained above, the remaining Y oxides are dissolved during the acid treatment and the Pt atoms re-arrange forming an overlayer of 1.2 nm. After activation, the Pt-skin thickness increases to 1.4 nm and the final thickness is ca 1.7 nm, which would correspond to 10 Pt atomic layers. Even though there is not a precise number when deliberating an optimal thickness for the Pt overlayer [50], previous measurements in literature reported that there is a correlation between the thickening of the Pt overlayer and ORR activity losses [51,52]. Escribano et al. [50] reported that beyond a certain level of bulk strain, the Pt overlayer is destabilized producing a decrease of the ORR activities, which correlates well with our electrochemical results. The small changes in Pt:Y bulk composition observed in EDX results are also in good agreement with an overly thick and presumably unstable Pt overlayer. The instability of the Pt overlayer results in an increased surface mobility that provides channels for the dissolution of residual Y atoms located in the vicinity, thereby reducing even more the amount of Y oxides on the Pt surface. However, as explained earlier, the

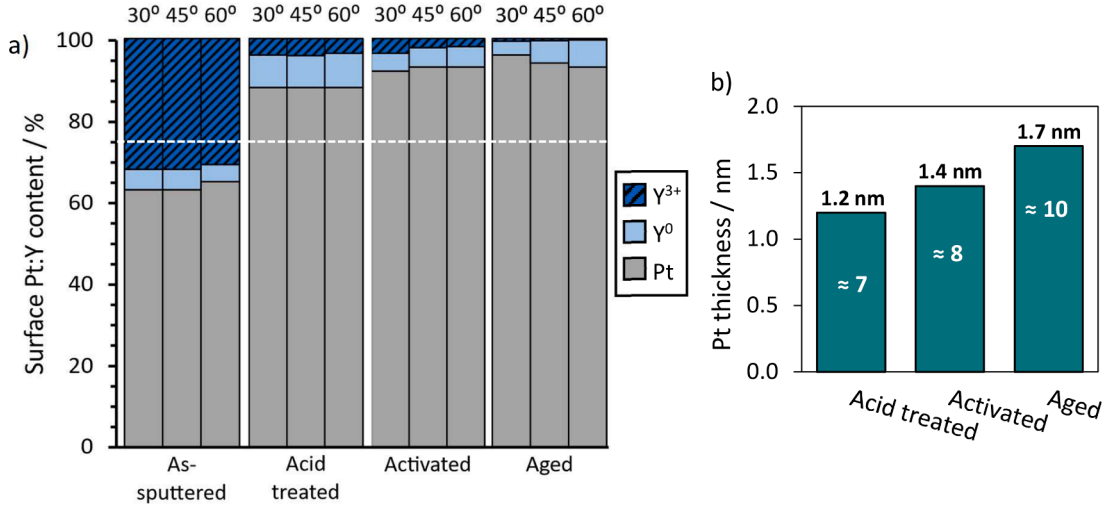

Fig. 5. a) Pt:Y surface content, as well as the amount of Y^0 (metallic state) and Y^{3+} (oxidized state) for each Pt_3Y sample measured at three different X-ray incident angles (30°, 45° and 60°) in AR-XPS. The dashed white line depicts the nominal alloy composition of the sputtered targets. b) Pt overlayer thickness in Pt_3Y samples estimated from XPS intensities. The white digits are the corresponding Pt atomic layers (approximated numbers).

Pt thickness determined from XPS quantification should be taken merely as an indication and conclusive statements shall not be drawn from these values.

In order to elucidate the change in Pt binding energy at different stages of the electrochemical testing, deconvolution of Pt-4f XPS spectra was conducted on both Pt and Pt_3Y samples at 30° (Y-3d spectra are in Supplementary information) to obtain a more surface-sensitive electronic structure insight. The deconvolution of XPS spectra in different Pt_3Y samples (Fig. 6a) reveals a steady surface composition of Pt species, namely metallic Pt (Pt^0) and oxidized Pt (Pt^{2+} and Pt^{4+}), which indicates that Pt corrosion is not responsible for the ORR activity decay observed in the aged samples (Fig. 3). More importantly, deconvolution of the Pt-4f XPS spectrum in the as-sputtered Pt_3Y sample shows a Pt^0 of a very different nature than that in the pure Pt sample (Fig. 6b), as evidenced by its significantly lower binding energy (70.7 eV). This value is remarkably lower than that reported in the literature for pure Pt [22,53,54], although in principle is in good agreement with the Pt-Y alloy formation that results in a withdrawal of Pt electronic density [16,55]. After acid treatment, a 0.1 eV shift towards higher binding energies is observed for all Pt species in Pt_3Y. This further proves a change in the d-band of surface Pt, which is ascribed to the formation of an unalloyed Pt-rich overlayer as described in Fig. 5b. We therefore infer that the activation step results in a surface Pt with an optimal binding energy of the oxygen-containing species, which in turn gives rise to the ORR activity enhancement observed for Pt_3Y in our electrochemical measurements. By the same principle, the noticeable decay in its ORR activity after the AST is explained in terms of Pt binding energy and thus O affinity, which correlates well with the ORR reactivity of the different geometries of the Pt active sites described in section 3.1.2. The Pt-4f XPS spectrum deconvolution reveals a prominent increase (0.15 eV) in Pt^0 binding energy after aging, which brings metallic Pt to 71.2 eV, very close to pure Pt (Fig. 6c). The Pt^0 binding energy similarities between aged Pt_3Y, and as-sputtered Pt is in very good accordance with the ORR specific activities observed in Fig. 3, where both catalysts show a very similar current response along a wide voltage range, which proves the similarities in the electronic structure of both samples. More importantly, we infer that this 0.15 eV positive shift in Pt^0 binding energy is more than sufficient to bring Pt in Pt_3Y back to the too strong O* adsorption catalyst category, which we attribute as the reason behind the observed ORR activity decrease. The aged Pt sample, however, exhibits a hardly noticeable negative shift (0.04 eV) in Pt^0 binding energy with respect to as-sputtered Pt, which is clearly not enough to explain the decrease of ORR activity observed in these samples. Because the electronic structure in pure Pt seems unaltered, Pt morphology upon aging was investigated to attempt to single out the cause of the decreased ORR activity after aging.

3.2.2. *Morphology*

The impact of AST on morphology of the sputtered Pt- and Pt_3Y thin films is shown in the high-resolution scanning electron microscopy (SEM) images in Fig. 7.

Fig. 7a shows the SEM picture of the as-sputtered Pt sample, before AST. As in SEM profiles for plasma sputtered Pt published by Brault et al. [56], Pt crystallites are distributed along the surface of the macroscopic MPL structure of the GDL forming a porous structure. In contrast with thin films deposited by using e-beam evaporation, DC magnetron

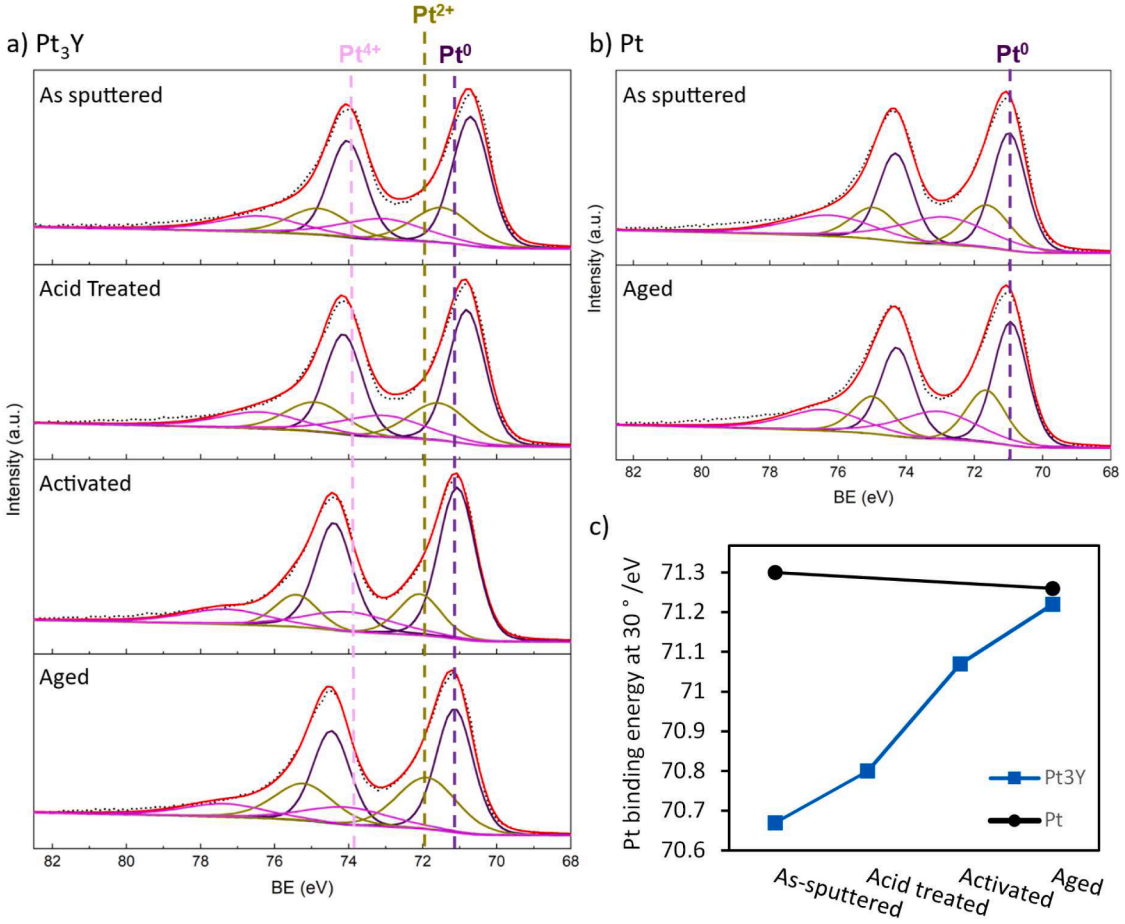

Fig. 6. Pt-4f XPS deconvoluted spectra at 30° with corresponding Pt surface species for a) Pt_3Y and b) Pt samples. c) Pt binding energy in both Pt and Pt_3Y of different samples measured in XPS at 30°

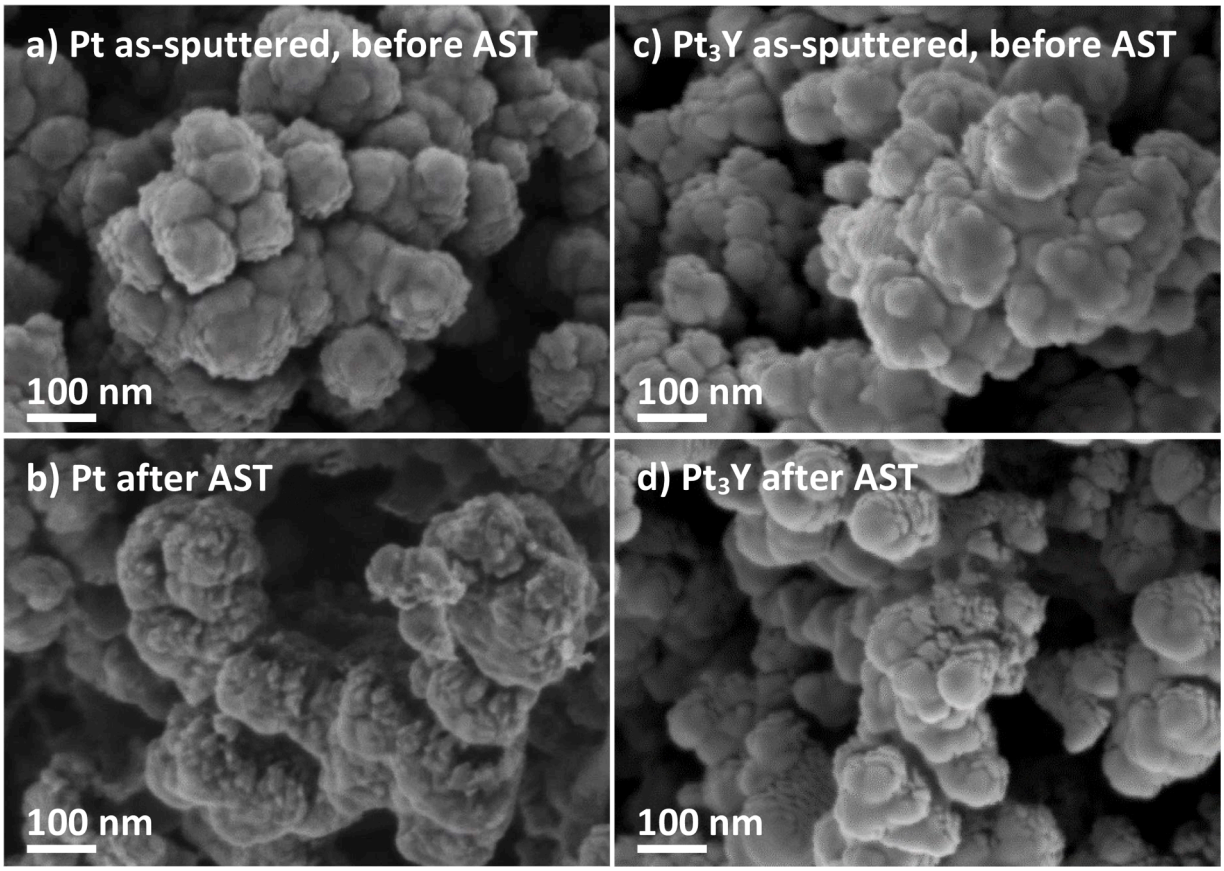

Fig. 7. SEM images of a) Pt as-sputtered before AST and b) Pt after AST. c) Pt_3Y as -sputtered, before AST and d) Pt_3Y after AST. All images were taken at 5 kV with backscattered electrons.

sputtering creates smaller Pt crystallites and, as the whole MPL surface is covered with Pt, the contrast difference in the image is low [57]. After AST, in Fig. 7b, a considerable growth of the Pt domains is observed and almost no small clusters are found at the surface of the catalyst film. As mentioned in Section 3.1.3, Pt dissolves and redeposits in PEMFCs during potential cycling conditions performed at a high scan rate [58]. Therefore, the growth of the Pt domains we observe for Pt after AST in Fig. 7b results from a Pt dissolution/redeposition process denominated in literature as Ostwald ripening [28]. Fig. 7c shows the morphology of the Pt_3Y as-sputtered sample. After deposition, the whole porous macrostructure of the MPL seems covered with Pt_3Y nano-clusters. The morphology of Pt_3Y after AST (Fig. 7d) appears to be rougher. However, this morphology is also observed in the Pt_3Y as-sputtered sample when SEM is performed with an angle-view of 45° (see Supplementary information). Hence, the morphology of Pt_3Y after AST is very similar to as-sputtered Pt_3Y before AST in this view, which indicates that the AST does not induce degradation in the morphology of the catalyst thin film itself.

3.2.3. *Microstructure*

TEM further confirms the differences in morphology of Pt_3Y thin films before and after AST to be very small. Fig. 8 depicts the microstructure of Pt_3Y thin film samples: as-sputtered (Fig. 8a), acid treated (Fig. 8b) and after AST (Fig. 8c). Imaging was performed in the transitional region between full film thickness and naked carbon support. Film thickness in this region varies depending on the degree of sputtered

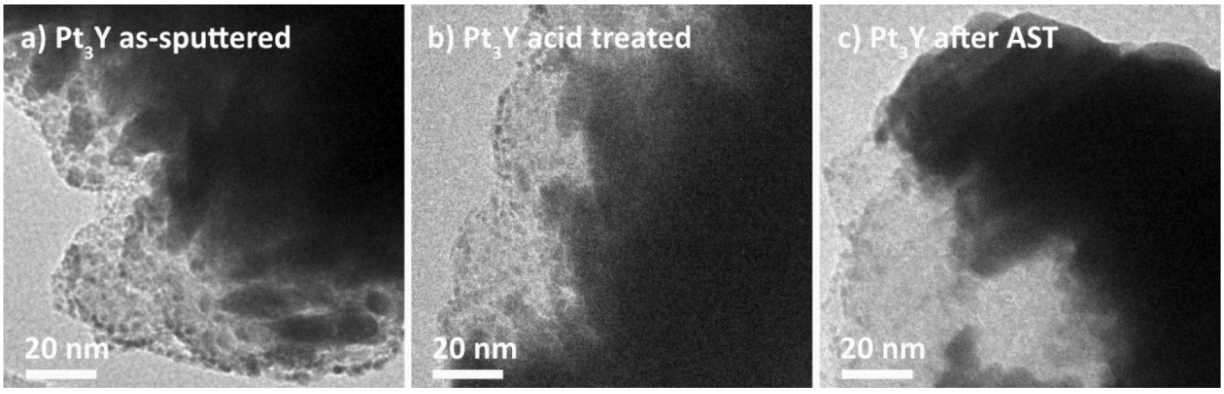

Fig. 8. TEM micrographs of a) Pt_3Y as-sputtered before AST, b) Pt_3Y acid treated, before AST and c) Pt_3Y after AST. All images were attained at 200 kV acceleration voltage.

material reaching the substrate, where dark areas of higher film thickness were originally oriented more towards the sputter target. Consequently, and in agreement with [21], full alloy film coverage is obtained on top of the carbon particles, while the sputtered catalyst layer decreases in thickness to eventually consist of separate nanoparticles on the sides of the carbon particles. No significant differences in film morphology of Pt_3Y samples before (Fig. 8a and 8b) and after (Fig. 8c) AST are observed in the TEM micrographs, suggesting that the continued leaching of yttrium during aging does not largely affect the microstructure of the alloy thin film.

4. Conclusions

In order to investigate the long-term ORR activity of Pt_3Y thin films in relevant fuel cell conditions, an accelerated stress test (AST) consisting of 3600 potential cycles between 0.4 and 1.4 V at 1 V s^{-1} was performed in a single proton exchange membrane fuel cell (PEMFC) at 80 °C and 100% RH. The impact of the AST was evaluated by analyzing the ORR activities obtained from polarization curves before and after the AST. The ECSA was measured by CO-stripping voltammetry, whereas the morphological changes were monitored by means of scanning electron microscopy (SEM) and transmission electron microscopy (TEM). Variations in surface compositions and electronic structures were evaluated by energy-dispersive X-ray spectroscopy (EDX) and X-ray photoelectron spectroscopy (XPS).

After AST, the polarization curves for both Pt and Pt_3Y are shifted downwards indicating loss of ORR activity at all voltages. Except at very high voltages ($E > 0.85$ V_{RHE}) the ORR activity of Pt_3Y after AST is very close to that of Pt before AST. This correlates well with the results from the deconvolution of Pt-4f XPS spectra where the binding energy of metallic Pt in Pt_3Y is very close to pure Pt (71.22 eV). The ECSA decrease due to AST is similar for both materials: around 16% for Pt and 17% for Pt_3Y. Similar morphologies are observed for aged Pt_3Y and as-sputtered Pt, and the EDX results confirm a steady bulk composition of Pt_3Y thin films throughout the entire electrochemical test. Based on all obtained results, we conclude that the loss of ORR activity for Pt_3Y is due to an increase in the thickness of the Pt overlayer. This induces a relaxation of the Pt overlayer, which in turn decreases the compressive strain effect. For pure Pt, the loss of ORR activity is due to a growth of the Pt domains associated with the Ostwald ripening process. Considering the obtained results, the AST presented is expected to be of great use when studying the stability of other Pt-alloys in PEMFCs.

CRediT authorship contribution statement

Eva Marra: Investigation, Methodology, Formal analysis, Writing – review & editing, Writing – original draft. **Gerard Montserrat-Sisó:** Methodology, Formal analysis, Writing – review & editing. **Björn Eriksson:** Investigation, Methodology, Writing – review & editing. **Björn Lönn:** Formal analysis, Writing – review & editing. **Rakel Wreland Lindström:** Supervision, Conceptualization, Writing – review & editing, Funding acquisition. **Göran Lindbergh:** Supervision, Conceptualization, Writing – review & editing, Funding acquisition. **Björn Wickman:** Supervision, Conceptualization, Writing – review & editing, Funding acquisition. **Carina Lagergren:** Supervision, Conceptualization, Writing – review & editing, Funding acquisition.

Declaration of Competing Interest

The authors declare that they have no known competing financial interests or personal relationships that could have appeared to influence the work reported in this paper.

Data availability

Data will be made available on request.

Acknowledgments

This work was supported by the Swedish Foundation for Strategic Research (SSF Project No. EM16–0060 and ARC19–0026), the Strategic Vehicle Research and Innovation program (FFI Project No. P37806–3), the Swedish governmental initiative StandUp for Energy, the Swedish Research Council (Project No. 2018–03927) and the Swedish Energy Agency. The authors also sincerely thank Dr. Rosemary Brown for the initial sputter deposition of the Pt samples.

Supplementary materials

Supplementary material associated with this article can be found, in the online version, at doi:10.1016/j.electacta.2023.143436.

References

[1] Y. Manoharan, et al., Hydrogen fuel cell vehicles; current status and future prospect, Appl. Sci. 9 (11) (Jun. 2019) 2296, https://doi.org/10.3390/app9112296.
[2] A.G. Olabi, T. Wilberforce, M.A. Abdelkareem, Fuel cell application in the automotive industry and future perspective, Energy 214 (Jan. 2021), 118955, https://doi.org/10.1016/j.energy.2020.118955.
[3] M. Kobayashi, Y. Tabe, T. Chikahisa, Analysis and experiments of major parameters in catalyst layer structure affecting on PEFC performance, ECS Trans. 50 (2) (Mar. 2013) 415–422, https://doi.org/10.1149/05002.0415ecst.
[4] A. Ostroverkh, et al., Optimization of ionomer-free ultra-low loading Pt catalyst for anode/cathode of PEMFC via magnetron sputtering, Int. J. Hydrogen Energy 44 (35) (Jul. 2019) 19344–19356, https://doi.org/10.1016/j.ijhydene.2018.12.206.
[5] K. Fu, et al., Magnetron sputtering a high-performance catalyst for ultra-low-Pt loading PEMFCs, J. Alloys Compd. 815 (Jan. 2020), 152374, https://doi.org/10.1016/j.jallcom.2019.152374.
[6] Y.J. Lee, et al., Ultra-Low Pt loaded porous carbon microparticles with controlled channel structure for high-performance fuel cell catalysts, Adv. Energy Mater. 11 (48) (Dec. 2021), 2102970, https://doi.org/10.1002/aenm.202102970.
[7] I. Farid, A. Boruah, J. Chutia, A.R. Pal, H. Bailung, Low loaded platinum (Pt) based binary catalyst electrode for PEMFC by plasma co-sputtered deposition method, Mater. Chem. Phys. 236 (Oct. 2019), 121796, https://doi.org/10.1016/j.matchemphys.2019.121796.
[8] R. Lin, L. Che, D. Shen, X. Cai, High durability of Pt-Ni-Ir/C ternary catalyst of PEMFC by stepwise reduction synthesis, Electrochim. Acta 330 (Jan. 2020), 135251, https://doi.org/10.1016/j.electacta.2019.135251.
[9] N. Shroti, M.K. Daletou, The Pt–Co alloying effect on the performance and stability of high temperature PEMFC cathodes, Int. J. Hydrogen Energy 47 (36) (Apr. 2022) 16235–16248, https://doi.org/10.1016/j.ijhydene.2022.03.109.
[10] C.A. Campos-Roldán, D.J. Jones, J. Rozière, S. Cavaliere, Platinum-rare earth alloy electrocatalysts for the oxygen reduction reaction: a brief overview, ChemCatChem 14 (19) (Oct. 2022), https://doi.org/10.1002/cctc.202200334.
[11] J. Greeley, et al., Alloys of platinum and early transition metals as oxygen reduction electrocatalysts, Nat. Chem. 1 (7) (Oct. 2009) 552–556, https://doi.org/10.1038/nchem.367.
[12] S.G. Peera, T.G. Lee, A.K. Sahu, Pt-rare earth metal alloy/metal oxide catalysts for oxygen reduction and alcohol oxidation reactions: an overview, Sustain Energy Fuels 3 (8) (2019) 1866–1891, https://doi.org/10.1039/C9SE00082H.
[13] S. Jong Yoo, et al., Enhanced stability and activity of Pt–Y alloy catalysts for electrocatalytic oxygen reduction, Chem. Commun. 47 (41) (2011) 11414, https://doi.org/10.1039/c1cc12448j.
[14] A.F. Pedersen, et al., Probing the nanoscale structure of the catalytically active overlayer on Pt alloys with rare earths, Nano Energy 29 (Nov. 2016) 249–260, https://doi.org/10.1016/j.nanoen.2016.05.026.
[15] S.J. Hwang, et al., Role of electronic perturbation in stability and activity of Pt-based alloy nanocatalysts for oxygen reduction, J. Am. Chem. Soc. 134 (48) (Dec. 2012) 19508–19511, https://doi.org/10.1021/ja307951y.
[16] P. Hernandez-Fernandez, et al., Mass-selected nanoparticles of PtxY as model catalysts for oxygen electroreduction, Nat. Chem. 6 (8) (Aug. 2014) 732–738, https://doi.org/10.1038/nchem.2001.
[17] R. Cui, et al., Facile synthesis of nanoporous Pt-Y alloy with enhanced electrocatalytic activity and durability, Sci. Rep. 7 (1) (Mar. 2017) 41826, https://doi.org/10.1038/srep41826.
[18] N. Lindahl, et al., High specific and mass activity for the oxygen reduction reaction for thin film catalysts of sputtered Pt $_3$ Y, Adv Mater Interfaces 4 (13) (Jul. 2017), 1700311, https://doi.org/10.1002/admi.201700311.
[19] E. Zamburlini, K.D. Jensen, I.E.L. Stephens, I. Chorkendorff, M. Escudero-Escribano, Benchmarking Pt and Pt-lanthanide sputtered thin films for oxygen electroreduction: fabrication and rotating disk electrode measurements, Electrochim. Acta 247 (Sep. 2017) 708–721, https://doi.org/10.1016/j.electacta.2017.06.146.
[20] R. Brandiele, et al., Climbing the oxygen reduction reaction volcano plot with laser ablation synthesis of Pt $_x$ Y nanoalloys, Catal. Sci. Technol. 10 (14) (2020) 4503–4508, https://doi.org/10.1039/D0CY00983K.

[21] N. Lindahl, et al., Fuel cell measurements with cathode catalysts of sputtered Pt_3Y thin films, ChemSusChem 11 (9) (May 2018) 1438–1445, https://doi.org/10.1002/cssc.201800023.

[22] B. Eriksson, et al., Enhanced oxygen reduction activity with rare earth metal alloy catalysts in proton exchange membrane fuel cells, Electrochim. Acta 387 (Aug. 2021), 138454, https://doi.org/10.1016/j.electacta.2021.138454.

[23] S. Stariha, et al., Recent advances in catalyst accelerated stress tests for polymer electrolyte membrane fuel cells, J. Electrochem. Soc. 165 (7) (May 2018) F492–F501, https://doi.org/10.1149/2.0881807jes.

[24] B.N. Popov and J. Weidner, "Development of ultra-low platinum alloy cathode catalysts for PEM fuel cells," Golden, CO (United States), Jan. 2016. doi: 10.2172/1330985.

[25] J.N. Schwämmlein, G.S. Harzer, P. Pfändner, A. Blankenship, H.A. El-Sayed, H. A. Gasteiger, Activity and stability of carbon supported Pt_xY alloys for the ORR determined by RDE and single-cell PEMFC measurements, J. Electrochem. Soc. 165 (15) (Oct. 2018) J3173–J3185, https://doi.org/10.1149/2.0221815jes.

[26] S.J. Yoo, et al., Pt3Y electrocatalyst for oxygen reduction reaction in proton exchange membrane fuel cells, Int. J. Hydrogen Energy 37 (12) (Jun. 2012) 9758–9765, https://doi.org/10.1016/j.ijhydene.2012.03.089.

[27] G.C. da Silva, N.A. Santos, J. Perez, Activity and long-term stability study of Pt-Y/C electrocatalysts for oxygen reduction reaction, ECS Trans. 72 (29) (Jul. 2016) 23–34, https://doi.org/10.1149/07229.0023ecst.

[28] J.C. Meier, et al., Degradation mechanisms of Pt/C fuel cell catalysts under simulated start–stop conditions, ACS Catal. 2 (5) (May 2012) 832–843, https://doi.org/10.1021/cs300024h.

[29] J. Speder, et al., Comparative degradation study of carbon supported proton exchange membrane fuel cell electrocatalysts – the influence of the platinum to carbon ratio on the degradation rate, J. Power Sources 261 (Sep. 2014) 14–22, https://doi.org/10.1016/j.jpowsour.2014.03.039.

[30] E. Zhu, et al., Stability of platinum-group-metal-based electrocatalysts in proton exchange membrane fuel cells, Adv. Funct. Mater. 32 (30) (Jul. 2022), 2203883, https://doi.org/10.1002/adfm.202203883.

[31] A.S. Aricò, et al., Performance and degradation of high temperature polymer electrolyte fuel cell catalysts, J. Power Sources 178 (2) (Apr. 2008) 525–536, https://doi.org/10.1016/j.jpowsour.2007.10.005.

[32] M. Luo, M.T.M. Koper, A kinetic descriptor for the electrolyte effect on the oxygen reduction kinetics on Pt(111), Nat. Catal. 5 (7) (Jul. 2022) 615–623, https://doi.org/10.1038/s41929-022-00810-6.

[33] P. Urchaga, S. Baranton, C. Coutanceau, G. Jerkiewicz, Electro-oxidation of CO_{chem} on Pt nanosurfaces: solution of the peak multiplicity puzzle, Langmuir 28 (7) (Feb. 2012) 3658–3663, https://doi.org/10.1021/la202913b.

[34] E.G. Ciapina, S.F. Santos, E.R. Gonzalez, Electrochemical CO stripping on nanosized Pt surfaces in acid media: a review on the issue of peak multiplicity, J. Electroanal. Chem. 815 (Apr. 2018) 47–60, https://doi.org/10.1016/j.jelechem.2018.02.047.

[35] P. Urchaga, S. Baranton, C. Coutanceau, Changes in COchem oxidative stripping activity induced by reconstruction of Pt (111) and (100) surface nanodomains, Electrochim. Acta 92 (Mar. 2013) 438–445, https://doi.org/10.1016/j.electacta.2013.01.042.

[36] I.J. McPherson, P.A. Ash, L. Jones, A. Varambhia, R.M.J. Jacobs, K.A. Vincent, Electrochemical CO oxidation at platinum on carbon studied through analysis of anomalous in situ IR spectra, J. Phys. Chem. C 121 (32) (Aug. 2017) 17176–17187, https://doi.org/10.1021/acs.jpcc.7b02166.

[37] L. Wang, et al., Core–shell nanostructured cobalt–platinum electrocatalysts with enhanced durability, ACS Catal. 8 (1) (Jan. 2018) 35–42, https://doi.org/10.1021/acscatal.7b02501.

[38] W. Luo, Y. Jiang, M. Wang, D. Lu, X. Sun, H. Zhang, Design strategies of Pt-based electrocatalysts and tolerance strategies in fuel cells: a review, RSC Adv. 13 (7) (2023) 4803–4822, https://doi.org/10.1039/D2RA07644F.

[39] H. Ekström, P. Hanarp, M. Gustavsson, E. Fridell, A. Lundblad, G. Lindbergh, A novel approach for measuring catalytic activity of planar model catalysts in the polymer electrolyte fuel cell environment, J. Electrochem. Soc. 153 (4) (2006), https://doi.org/10.1149/1.2170578.

[40] P. Ochal, et al., CO stripping as an electrochemical tool for characterization of Ru@Pt core-shell catalysts, J. Electroanal. Chem. 655 (2) (Jun. 2011) 140–146, https://doi.org/10.1016/j.jelechem.2011.02.027.

[41] C. Lim, et al., Membrane degradation during combined chemical and mechanical accelerated stress testing of polymer electrolyte fuel cells, J. Power Sources 257 (Jul. 2014) 102–110, https://doi.org/10.1016/j.jpowsour.2014.01.106.

[42] K. Higashi, et al., The relationship between the active Pt fraction in a PEFC Pt/C catalyst and the ECSA and mass activity during start-Up/Shut-down degradation by in situ time-resolved XAFS technique, J. Phys. Chem. C 121 (40) (Oct. 2017) 22164–22177, https://doi.org/10.1021/acs.jpcc.7b07264.

[43] I. Gerasimova, S. Belenov, N. Lyanguzov, I. Pankov, M. Tolstunov, A. Pavlets, Role of the potential range during stress testing of platinum-containing electrocatalysts at elevated temperature, Catalysts 12 (10) (Oct. 2022) 1179, https://doi.org/10.3390/catal12101179.

[44] A. Pavlišič, P. Jovanovič, V.S. Šelih, M. Šala, N. Hodnik, M. Gaberšček, Platinum dissolution and redeposition from Pt/C fuel cell electrocatalyst at potential cycling, J. Electrochem. Soc. 165 (6) (Mar. 2018) F3161–F3165, https://doi.org/10.1149/2.0191806jes.

[45] P. Malacrida, S. Horch, I. Chorkendorff, Alloys of Pt and Rare Earths for the Oxygen Electroreduction Reaction, Technical University of Denmark, 2014.

[46] L. Tang, et al., Electrochemical stability of nanometer-scale Pt particles in acidic environments, J. Am. Chem. Soc. 132 (2) (Jan. 2010) 596–600, https://doi.org/10.1021/ja9071496.

[47] R. Jinnouchi, E. Toyoda, T. Hatanaka, Y. Morimoto, First principles calculations on site-dependent dissolution potentials of supported and unsupported Pt particles, J. Phys. Chem. C 114 (41) (Oct. 2010) 17557–17568, https://doi.org/10.1021/jp106593d.

[48] J. Durst, et al., Reversibility of Pt-skin and Pt-skeleton nanostructures in acidic media, J. Phys. Chem. Lett. 5 (3) (Feb. 2014) 434–439, https://doi.org/10.1021/jz4025707.

[49] T.P. Johansson, et al., Towards the elucidation of the high oxygen electroreduction activity of Pt_xY: surface science and electrochemical studies of Y/Pt(111), Phys. Chem. Chem. Phys. 16 (27) (2014) 13718–13725, https://doi.org/10.1039/C4CP00319E.

[50] M. Escudero-Escribano, et al., Tuning the activity of Pt alloy electrocatalysts by means of the lanthanide contraction, Science (1979) 352 (6281) (Apr. 2016) 73–76, https://doi.org/10.1126/science.aad8892.

[51] R. Yang, J. Leisch, P. Strasser, M.F. Toney, Structure of dealloyed $PtCu_3$ thin films and catalytic activity for oxygen reduction, Chem. Mater. 22 (16) (Aug. 2010) 4712–4720, https://doi.org/10.1021/cm101090p.

[52] A. Velázquez-Palenzuela, et al., The enhanced activity of mass-selected Pt Gd nanoparticles for oxygen electroreduction, J. Catal. 328 (Aug. 2015) 297–307, https://doi.org/10.1016/j.jcat.2014.12.012.

[53] R. Brown, et al., Surface composition of a highly active Pt_3Y alloy catalyst for application in low temperature fuel cells, Fuel Cells 20 (4) (Aug. 2020) 413–419, https://doi.org/10.1002/fuce.201900186.

[54] C.A. Campos-Roldán, et al., Influence of the carbon support on the properties of platinum–yttrium nanoalloys for the oxygen reduction reaction, ACS Appl. Energy Mater. 5 (3) (Mar. 2022) 3319–3328, https://doi.org/10.1021/acsaem.1c03922.

[55] P. Malacrida, et al., Direct observation of the dealloying process of a platinum–yttrium nanoparticle fuel cell cathode and its oxygenated species during the oxygen reduction reaction, Phys. Chem. Chem. Phys. 17 (42) (2015) 28121–28128, https://doi.org/10.1039/C5CP00283D.

[56] P. Brault, et al., Plasma sputtering deposition of platinum into porous fuel cell electrodes, J. Phys. D.: Appl. Phys. 37 (24) (Dec. 2004) 3419–3423, https://doi.org/10.1088/0022-3727/37/24/010.

[57] E. Marra, et al., Oxygen reduction reaction kinetics on a Pt thin layer electrode in AEMFC, Electrochim. Acta 435 (Dec. 2022), 141376, https://doi.org/10.1016/j.electacta.2022.141376.

[58] N. Hodnik, et al., Severe accelerated degradation of PEMFC platinum catalyst: a thin film IL-SEM study, Electrochem. Commun. 30 (May 2013) 75–78, https://doi.org/10.1016/j.elecom.2013.02.012.